Escola de Primavera de Transição e Turbulência
Blumenau 2020

ABCM Associação Brasileira de Engenharia e Ciências Mecânicas

12th Spring School on Transition and Turbulence
September 21st-25th, 2020, Blumenau, SC, Brazil

EPTT-2020-0035
NUMERICAL ANALYSIS OF THE GEOMETRY INFLUENCE ON THE FLOW'S AERODYNAMIC PERFORMANCE IN ELEVATED BUILDINGS

Carlos Henrique Diedrich*
Vivian Machado†
Thiago Antonini Alves‡
Luiz Eduardo Melo Lima§
Department of Mechanics, Federal University of Technology—Paraná—, Ponta Grossa, PR 84017-220, Brazil
*chd145@hotmail.com,†vivian_machadoo@yahoo.com.br,‡antonini@utfpr.edu.br,§lelima@utfpr.edu.br

Abstract. *The height of buildings has become a relevant factor for the territory economy and higher accommodation of people, and this is due to the world population growth and density increase in large cities. The vertical rise of buildings has been restricted by structural limits and by the influence of winds operating in the higher regions. Currently, many technologies, such as the use of air conditioner and the geometries optimization, have enabled advances in the design of increasingly tall buildings. However, the structure built in very tall buildings makes them more subject to airflows. These airflows generate aerodynamic stresses that directly influence the structure stability. In this context, computational fluid dynamics is a tool widely used to analyze the influence of airflows in buildings. This tool kind provides extensive possibilities for evaluations and optimizations, using computers with processing capacity enough to the simulations, depending only on the limitations imposed by each software and the user experience. A numerical analysis was carried out in this work to study the influence of geometry in the simulation of high buildings with similar characteristics to the Shanghai World Financial Center. Thus, to demonstrate the importance of the airflow on the stability of structures, three distinct geometries were considered: structure A—sharp edges; structure B—roundness edges; structure C—similar to structure B but containing a central hole. The governing equations (Reynolds-averaged Navier–Stokes equations) were solved using the "Flow Simulation" package of the commercial software SOLIDWORKS®. Also, the k–ϵ turbulence model with damping functions and the semi-implicit method for pressure linked equations algorithm, for pressure–velocity coupling, were employed. The results of the simulations performed showed the values obtained from the acting forces and the pressure and velocity distributions, which prove the viability of the real structure of the building (structure C).*

Keywords: *numerical simulation, computational fluid dynamics, buildings*

1. INTRODUCTION

In areas of high urban density, the construction of buildings presents itself as the best solution for residential and commercial occupation. The creation of increasingly large structures has been a challenging task, and this has generated countless studies and analyses for building geometry optimizations (Miyashita *et al.*, 1993; Zhao *et al.*, 2011). Thus, to find the best features that provide structural security, combined with aesthetic and economic aspects, computational simulation is a tool for these objectives.

The Shanghai World Financial Center (SWFC), located in Pudong, a district of Shanghai in China, is listed among the eight highest buildings in the world and features an audacious structure measuring 494 m in height, where the wind velocity can reach 40 m/s (Zhao *et al.*, 2011). The wind velocity falling on the building surfaces generates a moment due to the distance with the turning center and, consequently, produces stresses on the structure. Due to its height and facade, wind loading is one of the controlling factors of the structural design of SWFC. An architectural detail present in the SWFC consists of a trapezoidal opening at the top of the building (Fig. 1). This opening presents itself as an alternative for minimizing structural efforts.

Zhao *et al.* (2011) presented a brief discussion about some wind engineering studies, comparing the wind loading obtained from wind tunnels and those predicted using Chinese codes. The main wind loading parameters, including the shape factor, Strouhal number, and terrain type, were discussed. The structural design considered for wind loading, design criteria, and the design wind parameters were determined. They concluded that the analysis and control of wind-induced vibration is one of the critical design topics for super tall buildings.

For stadium design, it is necessary to understand the interaction between wind and rain in several types of stadium geometry and its influence on the wetting of the stands. Hence, van Hooff *et al.* (2011) presented three-dimensional (3D) computational fluid dynamics (CFD) simulations of wind flow and wind-driven rain (WDR) for twelve different generic

Figure 1. Shanghai World Financial Center (GG001213, 2017).

stadium configurations that are representative of a wide range of current stadia. The steady-state Reynolds-averaged Navier–Stokes (RANS) simulations were employed to determine the wind-flow patterns. The Lagrangian particle tracking was applied to calculate the WDR trajectories, yielding the wetting pattern on the stands. Their investigation confirms the influence of overall stadium geometry and roof slope on the stand area that is wetted by WDR. It displays the sense of taking into account WDR in the stadium design process, and it provides some design guidelines to avoid this type of spectator discomfort.

Liu and Niu (2016) compared the performances of the RANS, large eddy simulation (LES), and detached eddy simulation (DES) modeling approaches in simulating the wind flow around an isolated building. Their study aimed at the turbulence model choice for precisely predicting outdoor microclimate and thermal comfort conditions in urban planning. The mean velocity fields on the building windward side predicted by the three models were in satisfactory agreement with the wind tunnel results. But, the LES and DES results were in more satisfying agreement with the experimental results for the leeward and lateral sides in both vertical and horizontal planes.

Du *et al.* (2017) studied the lift-up design effects in four standard building configurations on the wind comfort using CFD simulations. The comparisons between simulated results and wind tunnel data were applied to validate both the numerical method and the turbulence model. The mean wind velocity ratio and mean wind velocity change ratio are employed to recognize the wind comfort and to evaluate the improvements due to the lift-up design. Their results of simulations showed that the lift-up project can improve wind comfort in building surroundings and that its influence is highly dependent on the incident wind direction. Specifically, wind comfort is better under the oblique wind direction than the other two wind directions.

Hence, a CFD analysis was carried out in this work to study the geometry influence in the simulation of high buildings with similar characteristics to the Shanghai World Financial Center (SWFC). This work aims to show the importance of the airflow on the structure stability, considering three distinct geometries. The numerical results for the acting forces and the pressure and velocity distributions should demonstrate the most satisfactory building geometry.

2. MODEL

This section presents the definitions of the governing equations (Sect. 2.1) and the turbulence model (Sect. 2.2) for the computational model employed in this work.

2.1 Governing equations

Equations (1), (2), and (3) are the RANS equations and express the conservation of mass, momentum, and energy, respectively, in steady-state for incompressible flow (Tannehill *et al.*, 1997):

$$\frac{\partial \overline{u}_j}{\partial x_j} = 0 \tag{1}$$

$$\frac{\partial}{\partial x_j}\left(\rho \overline{u}_i \overline{u}_j + \widehat{p}\delta_{ij} - \overline{\tau}_{ij}^{\mathrm{tot}}\right) = 0 \tag{2}$$

$$\frac{\partial}{\partial x_j}\left[\left(\rho C_p \overline{T} - \widehat{p}\right)\overline{u}_j - \overline{\tau}_{ij}^{\mathrm{tot}}\overline{u}_i + \overline{q}_j^{\mathrm{tot}}\right] = 0 \tag{3}$$

Where x_i and $\overline{u}_i$ represent the position and velocity vectors, respectively, δ_{ij} is the Kronecker delta function, ρ is the density, C_p is the isobaric specific heat, and $\overline{T}$ is the absolute temperature.

The modified pressure $\widehat{p}$ has its definition given by Eq. (4):

$$\widehat{p} = \overline{p} + \rho g x_i \tag{4}$$

Where g is the gravitational acceleration. For an ideal gas, the static pressure is provided by $\overline{p} = \rho R\overline{T}$, with R being the gas constant.

The total (laminar and turbulent) viscous stress, $\overline{\tau}_{ij}^{\mathrm{tot}}$, and the total (laminar and turbulent) heat flux, $\overline{q}_j^{\mathrm{tot}}$, are given by Eqs. (5) and (6), respectively:

$$\overline{\tau}_{ij}^{\mathrm{tot}} \equiv \overline{\tau}_{ij}^{\mathrm{lam}} + \overline{\tau}_{ij}^{\mathrm{turb}} = (\mu + \mu_{\mathrm{t}}) \left(\frac{\partial \overline{u_i}}{\partial x_j} + \frac{\partial \overline{u_j}}{\partial x_i} \right) \tag{5}$$

$$\overline{q}_j^{\mathrm{tot}} \equiv \overline{q}_j^{\mathrm{lam}} + \overline{q}_j^{\mathrm{turb}} \approx -C_p \left(\frac{\mu}{\mathrm{Pr}} + \frac{\mu_{\mathrm{t}}}{\mathrm{Pr}_{\mathrm{t}}} \right) \frac{\partial \overline{T}}{\partial x_j} \tag{6}$$

Where μ and μ_{t} are the molecular and turbulent dynamic viscosities, respectively, and Pr and Pr_{t} are the laminar and turbulent Prandtl numbers, respectively.For air $\mathrm{Pr} \approx 0.71$, and a turbulence model is used to give values for μ_{t} as well as Pr_{t}, although $\mathrm{Pr}_{\mathrm{t}} \approx 0.9$ is usually employed.

For the cases studied in this work, the temperature variation is not significant, and the energy equation, Eq. (3), can be disregarded, considering the flow as isothermal.

2.2 Turbulence model

The modified k–ϵ turbulence model with damping functions proposed by Lam and Bremhorst (1981) describes laminar, turbulent, and transitional flows of homogeneous fluids, consisting of the two transport equations. The first for the turbulent kinetic energy k, Eq. (7), and the second for its dissipation rate ϵ, Eq. (8):

$$\frac{\partial}{\partial t}(\rho k) + \frac{\partial}{\partial x_j} \left[\rho k u_j - \left(\mu + \frac{\mu_{\mathrm{t}}}{\sigma_k} \right) \frac{\partial k}{\partial x_j} \right] = P_k + P_{\mathrm{b}} - Y_{\mathrm{Ma}} - \rho\epsilon \tag{7}$$

$$\frac{\partial}{\partial t}(\rho \epsilon) + \frac{\partial}{\partial x_j} \left[\rho \epsilon u_j - \left(\mu + \frac{\mu_{\mathrm{t}}}{\sigma_\epsilon} \right) \frac{\partial \epsilon}{\partial x_j} \right] = C_{1\epsilon} f_1 \left(P_k + C_{3\epsilon} P_{\mathrm{b}} \right) \frac{\epsilon}{k} - C_{2\epsilon} f_2 \rho \frac{\epsilon^2}{k} \tag{8}$$

Where σ_k and σ_ϵ are the turbulent Prandtl numbers for k and ϵ, respectively, and these constants are in Table 1. For steady-state, the time derivatives in Eqs. (7) and (8) can be eliminated, i.e., $\partial/\partial t = 0$.

The turbulent viscosity, μ_{t}, is calculated by combining k and ϵ, according to Eq. (9):

$$\mu_{\mathrm{t}} = C_\mu f_\mu \rho \frac{k^2}{\epsilon} \tag{9}$$

Where C_μ is a constant, and its value is in Table 1.

The kinetic energy production term due to the mean velocity gradients, P_k, is given by Eq. (10):

$$P_k = -\rho \overline{u_i' u_j'} \frac{\partial u_j}{\partial x_i} \equiv \mu_{\mathrm{t}} S^2 \tag{10}$$

Where S ($\equiv \sqrt{2 S_{ij} S_{ij}}$) is the modulus of the mean rate-of-strain tensor considering the Boussinesq hypothesis, i.e., $S_{ij} = (1/2)(\partial u_i/\partial x_j + \partial u_j/\partial x_i)$.

The kinetic energy production term due to buoyancy, P_{b}, is given by Eq. (11):

$$P_{\mathrm{b}} = g_i \beta \frac{\mu_{\mathrm{t}}}{\mathrm{Pr}_{\mathrm{t}}} \frac{\partial T}{\partial x_i} \tag{11}$$

Where g_i is the gravitational acceleration vector. For the standard k–ϵ model, the Pr_{t} default value is 0.85. By definition, the thermal expansion coefficient is $\beta = -(1/\rho)(\partial\rho/\partial T)_p$. For isothermal flow, the kinetic energy production term due to buoyancy can be eliminated, i.e., $P_{\mathrm{b}} = 0$.

The dilatation dissipation term, Y_{Ma}, is modeled by Eq. (12), according to Sarkar and Lakshmanan (1991):

$$Y_{\mathrm{Ma}} = 2\mathrm{Ma}_{\mathrm{t}}^2 \rho\epsilon \tag{12}$$

Where the turbulent Mach number is defined as $\mathrm{Ma_t} = \sqrt{k/a^2}$, by definition, and a ($\equiv \sqrt{\gamma RT}$, for an ideal gas) is the speed of sound, with γ being the ratio of specific heats, and R is the gas constant. For incompressible flow, the dilatation dissipation term can be eliminated, i.e., $Y_{\mathrm{Ma}} = 0$.

The damping functions introduced by Lam and Bremhorst (1981), f_μ, f_1, and f_2, are determined from Eqs. (13), (14), and (15), respectively:

$$f_\mu = \left(1 - e^{-A_\mu \mathrm{Re}_k}\right)^2 \left(1 + \frac{A_\mathrm{t}}{\mathrm{Re_t}}\right) \tag{13}$$

$$f_1 = 1 + \left(\frac{A_{C1}}{f_\mu}\right)^3 \tag{14}$$

$$f_2 = 1 - e^{\mathrm{Re_t^2}} \tag{15}$$

Where the turbulence Reynolds number based on the distance from a point to the wall, y, is determined by $\mathrm{Re}_k = k^{1/2}y/\nu$, and the default turbulence Reynolds number is given as $\mathrm{Re}_k = k^{1/2}y/\nu$ and $\mathrm{Re_t} = k^2/(\nu\epsilon)$. For both turbulence Reynolds numbers definitions, ν is the molecular kinematic viscosity. When $f_\mu = 1$, $f_1 = 1$, and $f_2 = 1$, the approach reverts to the original standard k–ϵ model proposed by Launder and Spalding (1974).

Table 1 presents the default values of the coefficients in the standard k–ϵ model, as well as in the damping functions, selected in the computational tool.

Table 1. Default values of the coefficients in the standard k–ϵ model and the damping functions.

$C_{1\epsilon}$	$C_{2\epsilon}$	$C_{3\epsilon}$	C_μ	σ_k	σ_ϵ	A_μ	A_t	A_{C1}
1.44	1.92	[a]	0.09	1.0	1.3	0.0165	20.5	0.05

[a] $0 \leq C_{3\epsilon} \leq 1$, but an approximation that satisfies both limits is $C_{3\epsilon} = \tanh|v/u|$, where v and u are the velocity components parallel and perpendicular to the gravitational vector, respectively (Henkes *et al.*, 1991).

3. NUMERICAL PROCEDURE

The "Flow Simulation" package of the commercial software SOLIDWORKS® was employed to run the numerical simulations in this work. This package uses computer-aided design (CAD) geometries without modifications in fluid dynamic simulations (type CAD-embedded CFD), which incorporates several technologies: CAD data management, mesh generation, CFD solvers, engineering modeling technologies, and processing of results (Sobachkin and Dumnov, 2014).

The wall treatment uses a novel and original two-scale wall function (2SWF) approach that consists of two methods for coupling the boundary layer calculation with the solution of the bulk flow (Sobachkin and Dumnov, 2014):

- A "thin" boundary layer treatment, when the number of cells across the boundary layer is not enough for direct or even simplified determination of the flow and thermal profiles.
- A "thick" boundary layer approach, when the number of cells across the boundary layer exceeds that required to resolve the boundary layer accurately.

For intermediate cases, a combination of these two approaches is employed in the wall treatment, ensuring a smooth transition between the two models with the mesh refinement, or as the boundary layer thickens along a surface (Sobachkin and Dumnov, 2014).

The pressure–velocity coupling is solved using the semi-implicit method for pressure linked equations (SIMPLE) algorithm (Patankar, 1980).

All simulations are performed in the Computational Research Laboratory, linked to the Graduate Program in Mechanical Engineering of the Federal University of Technology—Paraná—, taking only a few minutes to run using a computer with the following characteristics:

- Microsoft Windows® 7 (64-bit) operating system.
- Intel® Core™ i7–3770 (3.4 GHz) processor.
- 8 GB RAM.

The following sections introduce the descriptions and characteristics of the building geometries (Sect. 3.1), computational mesh (Sect. 3.2), and velocity profile (Sect. 3.3), considered in the numerical procedure.

3.1 Building geometries

This analysis considers three geometries for the building that are affected by the airflow dynamics. These three geometric models present scales based on real data from the SWFC building (Zhao *et al.*, 2011), as showed in Fig. 2. The three geometric models showed in Fig. 2 differ due to the following aspects:

1. Structure A—presents sharp edges and has its faces perpendicular to the ground.
2. Structure B—presents roundness edges and has a slight slope on the faces where most of the flow occurs.
3. Structure C—are similar to structure B but containing a relief hole.

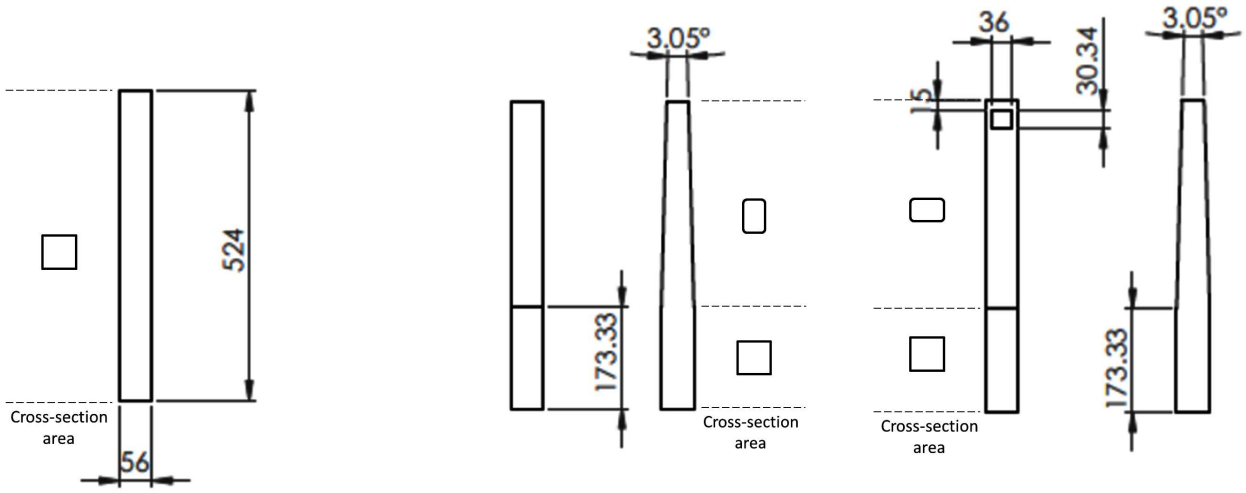

(a) (b) (c)

Figure 2. Building geometries: (a) structure A, (b) structure B, and (c) structure C.

3.2 Computational mesh

The computational meshes used to solve the problem are cartesian and comprise two different domains or control volumes (CV): flow (fluid) and structure (solid). The choice of mesh type is a consequence of the software used (in this case, a CAD-embedded CFD type), which has advantages such as simplicity, speed, and robustness of the mesh generation, as well as minimization of local truncation errors (Sobachkin and Dumnov, 2014). Table 2 summarizes the numbers of cells employed in each geometry mesh.

Table 2. Numbers of cells employed in each geometry mesh.

Cells	Structure A	Structure B	Structure C
Total	90800	90774	91448
Fluid	88496	88574	89038
Solid	2304	2200	2410
Partial	1200	1175	137

The software approach is to use an immersed-body mesh, i.e., the mesh starts independently from geometry itself, and the cells can arbitrarily intersect the boundary between solid and fluid. As a result of using cartesian-based meshes, it has cells that are located entirely in solid bodies (solid cells), in the flow (fluid cells), and cells intersected the immersed boundary (partial cells). In the simplest case, the partial cell consists of two CV: a fluid CV and a solid CV (Sobachkin and Dumnov, 2014).

The SOLIDWORKS® Flow Simulation tool was employed to create the computational meshes, and the meshes refinements were performed automatically according to the domain geometry and gradients in the solution. The domain limit is sufficient to capture the boundary layer around the structure. The surrounding reliefs (other buildings) can affect the results, but the building was considered isolated in these simulations. Figure 3 shows the computational meshes and structure refinement detail, as described in Table 2.

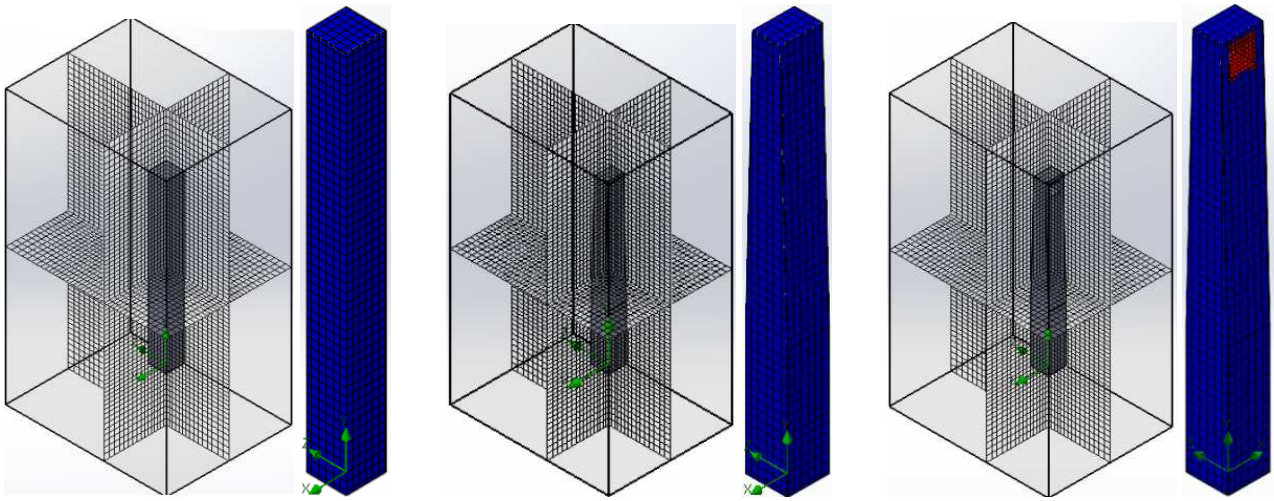

(a) (b) (c)

Figure 3. Computational meshes and structure refinement detail: (a) structure A, (b) structure B, and (c) structure C.

3.3 Velocity profile

According to Lamb and Kwok (2017), a power-law function defines the airflow velocity profile, which can be described by Eq. (16):

$$u(y) = u_0 \left(\frac{y}{y_0} \right)^n \tag{16}$$

Where u and u_0 are the local and reference velocities, respectively, y is the vertical coordinate, y_0 is the height for the reference velocity, and n is the power-law exponent dependent on the terrain type.

For all simulations performed, the power-law exponent (n) was considered as 0.6, because it is the factor that is more aggressive concerning the profile defined by Eq. (16). The average velocity is an input parameter employed in the simulations. Hence, 29.6 m/s was the value estimated from Eq. (16) for this input parameter. The velocity profile described by Eq. (16) corresponds to the inlet velocity at a boundary perpendicular to the relief hole. The other boundary conditions are considered as a free flow.

4. RESULTS AND DISCUSSION

The wind load is the resulting force due to the wind blowing against a building. The wind load depends on the wind velocity and the shape of the building. The structural design of the building must absorb wind forces safely and efficiently and transfer them to the foundations to prevent structural collapse. When investigating tall buildings employing wind engineering, the wind is frequently the dominant load and is essentially a horizontal force. Structural systems that receive wind loads tend to be separated from those for dead loads and other gravity loads produced internally for the building.

This section presents the results obtained for the comparisons of airflow's dynamic parameters (Sect. 4.1), as well as for the velocity trajectories and absolute pressure distributions (of fields) of the airflow around each structure (Sect. 4.2).

4.1 Dynamic parameters comparisons

Table 3 presents the numerical results of the airflow dynamic parameters for each structure considered in this work. These dynamic parameters are the forces and torque acting on the surfaces perpendicular (XY-plane) and tangent (ZY-plane) to the main direction of the airflow, as well as the frictional force.

Table 3. Forces or torque applied on the surfaces of the structures.

Force or torque	Unit	Structure A	Structure B	Structure C
Frictional force	N	0.046	0.042	0.053
Force perpendicular to ZY-plane	N	0.002	0.003	0.005
Force perpendicular to XY-plane	N	14.128	13.894	13.355
Torque perpendicular to X-axis	N m	3.702	3.605	3.355

Table 4 presents the same results of Table 3 but with each force (or torque) value being normalized by the corresponding value for the structure A, considered here as a reference because it is the most regular geometry.

Table 4. Normalized forces or torque applied on the surfaces of the structures.

Normalized force or torque	Structure A	Structure B	Structure C
Frictional force	1	0.91	1.15
Force perpendicular to ZY-plane	1	1.50	2.50
Force perpendicular to XY-plane	1	0.98	0.94
Torque perpendicular to X-axis	1	0.97	0.91

As expected, the force perpendicular to XY-plane presents the highest values as a consequence of the pressure drag, and theses values decrease from structure A to structure C, passing by structure B. The torque perpendicular to X-axis presents a similar behavior. On the other hand, the force perpendicular to ZY-plane increase from structure A to structure C, passing by structure B; even so, it presents negligible values in comparison with other acting forces.

4.2 Velocity trajectories and absolute pressure distributions

Figure 4 presents the velocity trajectories distribution (of field) around each structure considered in this work.

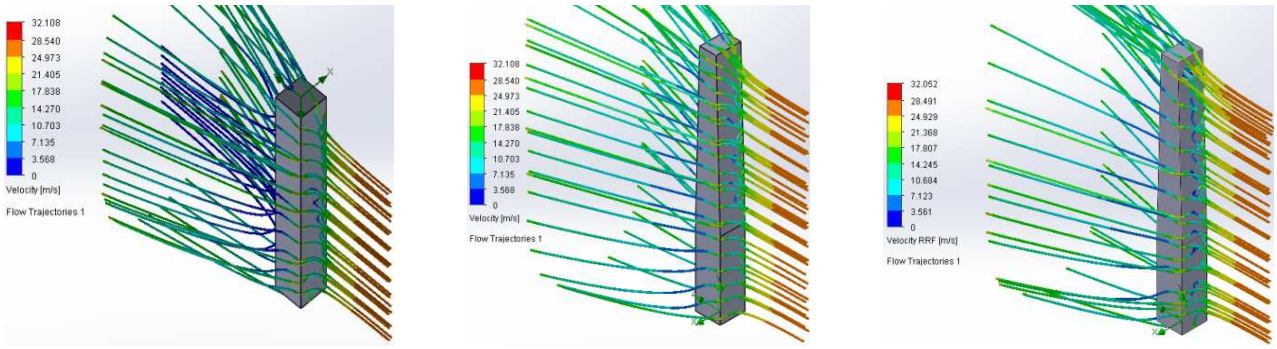

(a) (b) (c)

Figure 4. Velocity trajectories distribution in m/s: (a) structure A, (b) structure B, and (c) structure C.

It is possible to notice in Fig. 4c that the hole presence in the structure C causes a flow pathlines deviation, leaving the lines closer after passing through the hole.

Figure 5 presents the absolute pressure distribution (of field) around each structure considered in this work.

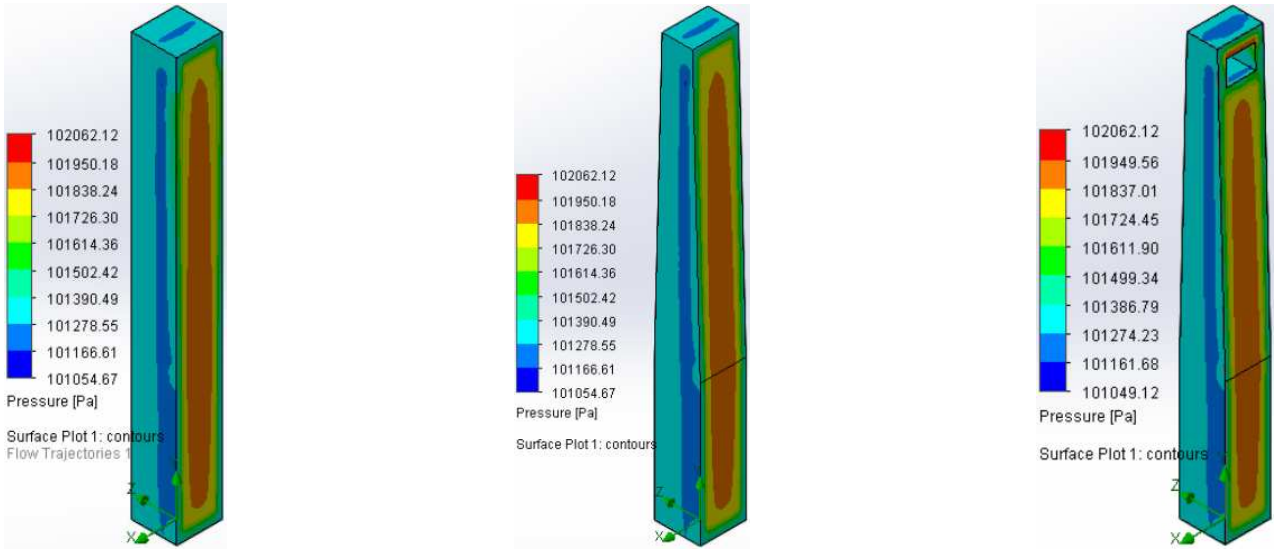

(a) (b) (c)

Figure 5. Absolute pressure distribution in Pa: (a) structure A, (b) structure B, and (c) structure C.

It is possible to notice in Fig. 5c that the hole presence in the structure C reduces the total area subject to the highest absolute pressure values, thereby decreasing pressure drag.

5. CONCLUSIONS

The CFD usage did it possible to find the pressure distributions and demonstrate that in all airflows around bodies, the side subject to the airflow has a pressure increase, and the opposite side generates a low-pressure area. This effect produces a secondary airflow at the body back necessary to cause this pressure to decrease.

The results show that the torsion moment and perpendicular force decreases with the edges rounding and the presence of the hole; nevertheless, the frictional force increases due to the increase in the contact surface area. Considering the same scale, the increase in frictional force is less than the reduction in perpendicular force and torsion moment.

Torque is the moment to rotate around the attachment point. In a building, this represents the total length below the surface. Using structure A as a reference, there was a torque decrease by approximately 3% for structure B and 9% for structure C, which can generate a reduction in construction cost.

In comparison with structure A, the frictional force decreases by about 9% for structure B and increases by about 15% for structure C, due to the increased total surface area resulting from the hole presence.

A comparison with a real model, or in scale, could improve the accuracy of the results. The usage and comparison with other CFD tools also can provide an alternative for results improving.

6. ACKNOWLEDGEMENTS

The authors thank the Federal University of Technology—Paraná—for the resources made available.

7. REFERENCES

Du, Y., Mak, C.M., Liu, J., Xia, Q., Niu, J. and Kwok, K.C.S., 2017. "Effects of lift-up design on pedestrian level wind comfort in different building configurations under three wind directions". *Build. Environ.*, Vol. 117, pp. 84–99. ISSN 0360-1323. DOI 10.1016/j.buildenv.2017.03.001.

GG001213, 2017. "The Shanghai International Finance Center, taken from the 118th floor of the Shanghai Center". Wikimedia Commons, the free media repository. URL https://commons.wikimedia.org/wiki/File:%E4%B8%8A%E6%B5%B7%E5%9B%BD%E9%99%85%E9%87%91%E8%9E%8D%E4%B8%AD%E5%BF%83.jpg.

Henkes, R.A.W.M., Van Der Vlugt, F.F. and Hoogendoorn, C.J., 1991. "Natural-convection flow in a square cavity calculated with low-Reynolds-number turbulence models". *Int. J. Heat Mass Transfer*, Vol. 34, No. 2, pp. 377–388. ISSN 0017-9310. DOI 10.1016/0017-9310(91)90258-G.

Lam, C.K.G. and Bremhorst, K., 1981. "A modified form of the k–ϵ model for predicting wall turbulence". *J. Fluids Eng.*, Vol. 103, No. 3, pp. 456–460. ISSN 0098-2202. DOI 10.1115/1.3240815.

Lamb, S. and Kwok, K.C.S., 2017. "The fundamental human response to wind-induced building motion". *J. Wind Eng. Ind. Aerodyn.*, Vol. 165, pp. 79–85. ISSN 0167-6105. DOI 10.1016/j.jweia.2017.03.002.

Launder, B.E. and Spalding, D.B., 1974. "The numerical computation of turbulent flows". *Comput. Methods Appl. Mech. Eng.*, Vol. 3, No. 2, pp. 269–289. ISSN 0045-7825. DOI 10.1016/0045-7825(74)90029-2.

Liu, J. and Niu, J., 2016. "CFD simulation of the wind environment around an isolated high-rise building: an evaluation of SRANS, LES and DES models". *Build. Environ.*, Vol. 96, pp. 91–106. ISSN 0360-1323. DOI 10.1016/j.buildenv.2015.11.007.

Miyashita, K., Katagiri, J., Nakamura, O., Ohkuma, T., Tamura, Y., Itoh, M. and Mimachi, T., 1993. "Wind-induced response of high-rise buildings effects of corner cuts or openings in square buildings". *J. Wind Eng. Ind. Aerodyn.*, Vol. 50, pp. 319–328. ISSN 0167-6105. DOI 10.1016/0167-6105(93)90087-5.

Patankar, S.V., 1980. *Numerical Heat Transfer and Fluid Flow*. Series in Computational Methods in Mechanics and Thermal Sciences. Hemisphere Publ. Co., New York, NY, 1st edition. ISBN 9780891165224.

Sarkar, S. and Lakshmanan, B., 1991. "Application of a Reynolds stress turbulence model to the compressible shear layer". *AIAA J.*, Vol. 29, No. 5, pp. 743–749. ISSN 1533-385X. DOI 10.2514/3.10649.

Sobachkin, A. and Dumnov, G., 2014. "Numerical basis of CAD-embedded CFD". In *NAFEMS World Congress 2013*. Dassault Systèmes, pp. 9–12. URL https://www.solidworks.com/sw/docs/Flow_Basis_of_CAD_Embedded_CFD_Whitepaper.pdf. White Paper.

Tannehill, J.C., Anderson, D.A. and Pletcher, R.H., 1997. *Computational Fluid Mechanics and Heat Transfer*. Series in Computational and Physical Processes in Mechanics and Thermal Sciences. Taylor & Francis Group, Washington, DC, 2nd edition. ISBN 9781560320463.

van Hooff, T., Blocken, B. and van Harten, M., 2011. "3D CFD simulations of wind flow and wind-driven rain shelter in sports stadia: influence of stadium geometry". *Build. Environ.*, Vol. 46, No. 1, pp. 22–37. ISSN 0360-1323. DOI 10.1016/j.buildenv.2010.06.013.

Zhao, X., Ding, J.M. and Suna, H.H., 2011. "Structural design of Shanghai Tower for wind loads". *Procedia Eng.*, Vol. 14, pp. 1759–1767. ISSN 1877-7058. DOI 10.1016/j.proeng.2011.07.221. The Proceedings of the Twelfth East Asia-Pacific Conference on Structural Engineering and Construction.

8. RESPONSIBILITY NOTICE

The authors are the only responsible for the printed material included in this paper.